# Phenomenology of the Low-Frequency Variability in a Reduced-Gravity, Quasigeostrophic Double-Gyre Model

JOHN D. MCCALPIN

*The Graduate College of Marine Studies, University of Delaware, Newark, Delaware*

DALE B. HAIDVOGEL

*Institute for Marine and Coastal Sciences, Rutgers University, New Brunswick, New Jersey*

## ABSTRACT

The low-frequency variability of the oceanic wind-driven circulation is investigated by use of a reduced-gravity, quasigeostrophic model with slight variations on the classic double-gyre wind forcing. Approximately 30 eddy-resolving simulations of 100–1000 years duration are analyzed to determine the types of low-frequency variability and to estimate statistical uncertainties in the results.

For parameters close to those leading to a stable antisymmetric solution, the system appears to have several preferred phenomenological regimes, each with distinct total energy levels. These states include a high-energy quasi-stable state; a low-energy, weakly penetrating state; and a state of intermediate energy and modest eddy/ring generation. The low-frequency variability of the model is strongly linked to the irregular transitions between these dynamical regimes.

For a central set of reference parameters, the behavior of the system is investigated for each period in which the total energy remains in certain ranges. The structure of the time-averaged streamfunction and eddy energy fields are observed to have remarkable repeatability from event to event for each state.

A parameter study documents the ways in which the probability distribution function of the total energy depends on the strength and asymmetry of the wind forcing field. As the parameters shift away from those leading to a steady antisymmetric solution, we find that increasing the asymmetry of the wind field or reducing the viscosity decreases the occurrences of the high-energy, quasi-stable state. The low-energy, weakly penetrating state is more robust and exists whenever there is both instability and a certain minimal asymmetry in the forcing. As the wind asymmetry is increased, the distributions shift smoothly (but rapidly) away from the higher-energy states, until only the low-energy state remains.

## 1. Introduction

The rectangular-basin, midlatitude, double-gyre model is the prototype most often used for the study of the dynamics of the midlatitude, wind-driven ocean circulation. Numerical simulations of single- and double-gyre oceans have been used to study the effects of the addition of nonlinearity to the classical Stommel and Munk models (Bryan 1963; Veronis 1966); the influence of topography on the gyre-scale circulation (Holland 1973; Verron et al. 1987); the role of eddies in the oceanic circulation and fluxes (Holland 1978); the influence of nonuniform winds (Rhines and Schopp 1991; Verron and LeProvost 1991); the separation of the western boundary current (Chassignet and Gent 1991; Haidvogel et al. 1992); and other topics.

A standard analysis of these simulations makes use of a separation of the solution into a time-independent "mean" field and a time-dependent "eddy" field. This separation is then used to derive and define the mean and eddy transport streamfunctions, the mean and eddy fluxes, and the mean and eddy energetics and associated energy transfers. In a previous paper, McCalpin (1995) examined the extent to which unresolved low-frequency variability introduced statistical uncertainties in the estimates of time averages of globally integrated measures (such as total energy) of a simple wind-driven ocean model. Here we investigate the phenomenology that gives rise to that low-frequency variability. We again make use of the reduced-gravity quasigeostrophic model because it contains the essential mechanisms of Rossby waves, wind forcing, barotropic instability, and damping, while simultaneously being computationally inexpensive enough to allow a large number of simulations of (typically) two centuries duration. The classical double-gyre forcing was chosen in order to provide a free jet analogous to the Gulf Stream.

*Corresponding author address:* Dr. John D. McCalpin, College of Marine Studies, University of Delaware, Robinson Hall, Newark, DE 19716-3501.

TABLE 1. Wind asymmetry parameter, $\alpha$, wind stress magnitude, $\tau$, and run number for the major cases discussed in this study. For each ($\tau$, $\alpha$) pair, a three-digit run number indicates that a simulation was run, most of the 200-year duration, while asterisks indicate that no simulation was performed. The reference case is run 104.

| $\tau$ | $\alpha$ | | | | | | | | |
|---|---|---|---|---|---|---|---|---|---|
| | 0.000 | 0.010 | 0.025 | 0.050 | 0.060 | 0.070 | 0.080 | 0.100 | 0.150 |
| 0.050 | 108 | 115 | 116 | 104 | 128 | 129 | 130 | 102 | 107 |
| 0.075 | 117 | 119 | * | 105 | * | * | * | 123 | 125 |
| 0.100 | 118 | 120 | * | 106 | * | * | * | 124 | 126 |

We show that, in some regions of parameter space, the system admits multiple persistent phenomenological regimes. In these regions, strong low-frequency variability is generated by infrequent transitions among the available states. Our approach is conceptually similar to recent work by Cessi and Ierley (1995) and Jiang et al. (1995) on multiple equilibrium solutions of the barotropic quasigeostrophic equations and the reduced-gravity shallow water equations, respectively, in the context of the wind-driven double-gyre model. Our system differs in that our solutions are strongly time-dependent and likely chaotic. Because of the absence of closed form solutions (or even descriptions) of the multiple persistent states, our discussion is necessarily less formal and more descriptive. We focus on a description of the phenomenology and speculations on the mechanisms that allow each of the regimes to persist, with particular emphasis on how the phenomenology and governing dynamical balances change with variations in the model parameters.

## 2. Model description

The model is an extension of that described briefly in McCalpin (1987) and more fully in McCalpin (1995).[1] The vertical structure of the fluid is assumed to be two immiscible, homogeneous layers of slightly different densities. The lower layer is assumed to be infinitely deep and at rest. The model uses standard second-order finite-difference methods to approximately solve the quasigeostrophic vorticity equation for the upper-layer flow

$$(\nabla^2 - \gamma^2)h_t + \beta h_x = -\frac{g'}{f_0} J(h, \nabla^2 h)$$

$$- r\nabla^2 h - A_b\nabla^6 h + \frac{f_0}{\rho_0 g' H} \text{curl}\vec{\tau}, \quad (1)$$

where $h$ is the interface anomaly (positive upward), $r$ is the coefficient of interfacial friction, $A_b$ is the coefficient of high-order (biharmonic) viscosity (also re-

ferred to as "hyperviscosity"), $\tau$ is the wind stress on the ocean surface, $\rho_0$ is the mean density of seawater, and $H$ is the reference thickness of the upper layer. The subscripts $x$ and $t$ indicate partial derivatives. Other definitions and standard numerical values include

$$r = 10^{-7} \text{ s}^{-1},$$

$$A_b = 8 \times 10^{10} \text{ m}^4 \text{ s}^{-1},$$

$$f_0 = 7.27 \times 10^{-5} \text{ s}^{-1},$$

$$\beta = 1.98 \times 10^{-11} \text{ m}^{-1} \text{ s}^{-1},$$

$$f = f_0 + \beta y,$$

$$\gamma^2 = \frac{f_0^2}{g'H} = (47636)^{-2} \text{ m}^{-2},$$

$$g' = g\frac{\Delta\rho}{\rho_0} = 0.02 \text{ m s}^{-2},$$

$$\beta = \frac{\partial f}{\partial y} = 1.97 \times 10^{-11} \text{ m}^{-1} \text{ s}^{-1},$$

$$J(a, b) = \frac{\partial a}{\partial x}\frac{\partial b}{\partial y} - \frac{\partial a}{\partial y}\frac{\partial b}{\partial x},$$

$$\nabla^2 a = \frac{\partial^2 a}{\partial x^2} + \frac{\partial^2 a}{\partial y^2},$$

$$\nabla^6 a = \nabla^2(\nabla^2(\nabla^2 a)).$$

In the above, $f$ is the Coriolis parameter (defined to be a linear function of $y$), $f_0$ is the value of the Coriolis parameter at the middle of the domain, $g$ is the gravitational acceleration, and $\Delta\rho$ is the difference between the layer densities.

The finite-difference approximation to the governing equation, (1), is solved in a domain of 3600 km (E–W) by 2800 km (N–S) extent using a uniform 20-km grid. The elliptic equation to recover the streamfunction at each time step is solved by a direct solver based on discrete sine transforms, yielding typically 11 significant digits of accuracy for the grid sizes used here. In all cases a free-slip boundary condition is used, with a higher-order boundary condition forcing no net momentum input from the high-order lateral viscous terms. Other features of the model are discussed in McCalpin (1995).

[1] A 70-page technical report describing the model and containing the full source code is available from the authors in either hard-copy or machine-readable format.
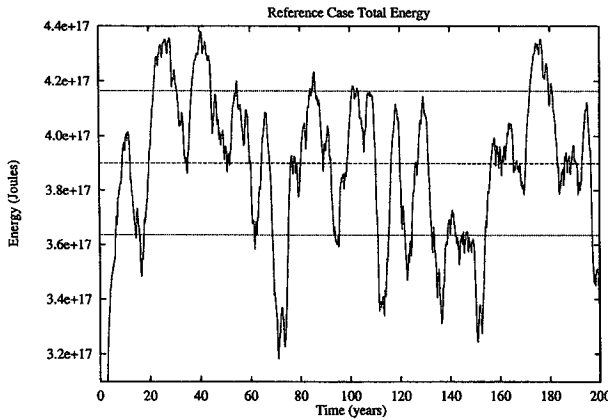
FIG. 1. Total energy time series for the first 200 years of the reference case. The horizontal lines indicate the sample mean and its standard deviation.

## 3. The reference case

We first describe the results from the reference case (run 104 of Table 1) in some detail. Discussions of the changes in phenomenology as the parameters are changed will follow in subsequent sections. The parameters for the reference case were chosen to balance strong jet penetration with significant meandering and eddy generation. In order to avoid problems with the spurious symmetry of the quasigeostrophic (QG) equations, the wind stress was made slightly asymmetric, with a curl field defined by

$$\text{curl}\vec{\tau} = \frac{\partial \tau^x}{\partial y} = \tau_0 \frac{2\pi}{L_y} \sin\left(2\pi \frac{y}{L_y}\right)$$

$$\times \left[1 - 4\alpha\left(\frac{y}{L_y} - \frac{1}{2}\right)\right], \quad (2)$$

where $0 < y < L_y$ is the meridional distance from the southern boundary of the basin. The reference value of $\tau_0$ is 0.05 N m$^{-2}$, which (in conjunction with the free-slip boundary conditions and the linear interfacial drag coefficient of $r = 10^{-7}$ s$^{-1}$) leads to maximum upper-layer velocities of about 0.60 m s$^{-1}$. The reference case employs a value of $\alpha = 0.05$, which increases the peak wind stress curl in the southern gyre by 5% and decreases the peak wind stress curl in the northern gyre by 5%, relative to the standard double-gyre configuration.

Values of $\alpha$ of the order of the Rossby number should be expected to provide a simulation of the effect of varying layer thickness in a more dynamically complete model, and in fact, the reference value of $\alpha = 0.05$ results in mean streamfunction patterns very similar to those obtained from the linear balance equations by McWilliams et al. (1990), which are, in turn, very similar to those for the primitive equations.

The reference case was run for 1000 years, and the statistics of the flow field were saved at 5-day intervals. For clarity, only the first 200 years of the total energy time series are presented in Fig. 1—the remaining 800 years are visually similar, and the statistical measures of the system for the first 200 years do not differ qualitatively from the statistics of the full 1000-year record. An interesting characteristic of this time series is the long duration of the periods of anomalous total energy. Such behavior is suggestive of a system with multiple preferred states, a suspicion reinforced by examination of the total energy histogram, Fig. 2, which represents the entire 1000-year integration. We see the most common energy near $3.9 \times 10^{17}$ J, with a low-energy peak near $3.5 \times 10^{17}$ J, and definite signs of one or more high-energy peaks in the range of $4.2 \times 10^{17}$–$4.3 \times 10^{17}$ J.

Figure 3 provides an estimate of the spectrum of the variability of the total energy series from the reference case. This spectrum is based on 71 280 five-day samples of the total energy, or about 990 years of model output. The spectral estimation and error bounds are obtained by the Welch method (using the MATLAB™ routine SPECTRUM). The decade from $10^{-3}$ to $10^{-2}$ cycles per year is based on a single Hanning window for the entire series, so that no error estimates are available. The decade from $10^{-2}$ to $10^{-1}$ cycles per year (and its associated 95% confidence intervals) is based on 10 bins of length 7128 samples and a Hanning window on each bin. The range above $10^{-1}$ cycles per year is based on 144 bins of length 495 samples and a Hanning window on each bin.

The spectrum appears roughly flat below a frequency below 0.1 cycles per year, and falls off rather quickly at higher frequencies, with a slope of $-2.5$ at periods
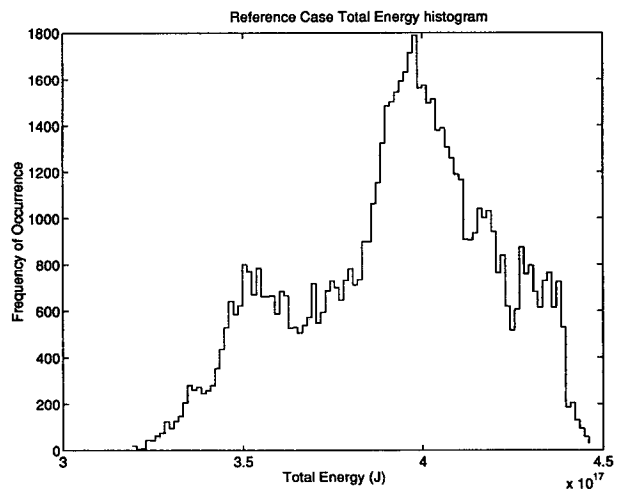


FIG. 2. Histogram of the total energy distribution for 990 years of the reference case. The preferred low-energy state is clearly visible near $3.5 \times 10^{17}$ J, and there are indications of one or two preferred high-energy states near $4.2 \times 10^{17}$ J and $4.3 \times 10^{17}$ J.
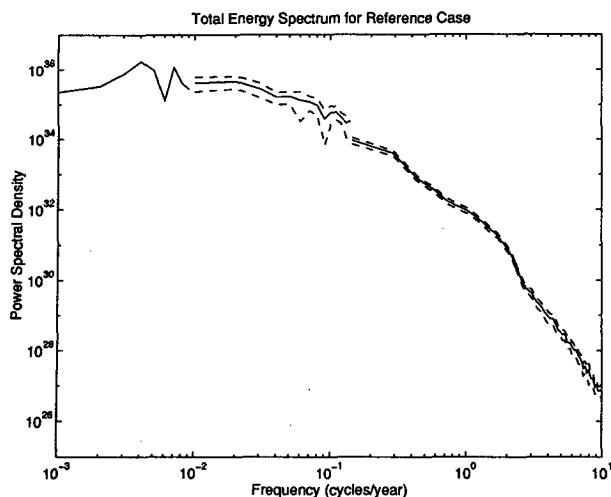
FIG. 3. Estimate of the power spectrum and 95% confidence intervals of the variability of the total energy from the reference case (run 104). The low-frequency end of the spectrum shows a level spectral energy density. See text for discussion.

slightly longer than annual and $-5.0$ at periods slightly shorter than annual. The change in slope corresponds to a mesoscale peak at about 2 cycles per year. There is no evidence of structure at any low frequency (though the uncertainty in the spectral estimates is large in the lowest decade). The timescale for long Rossby waves to cross the basin is 2.59 years, and the absence of any peaks in the 0.1 cycle per year to 1.0 cycle per year range suggests that basin modes are not relevant to the energetics of this system.

### a. Anomalous periods

We begin our analysis of the system by contrasting the behavior of the system during three periods of anomalously high total energy (near years 25, 40, and 175) with three periods of anomalously low total energy (near years 70, 110, and 150) and two periods of medium energy (near years 160 and 190). For each period, the time-averaged streamfunction is calculated, and the eddy kinetic energy (EKE) density and eddy potential energy (EPE) density fields are defined, according to

$$\text{EKE} \equiv \overline{\text{KE}(\psi')} = \frac{H\rho_0}{2}\frac{1}{T}\int_0^T (u'^2 + v'^2)dt \quad (3)$$

and

$$\text{EPE} \equiv \overline{\text{PE}(\psi')} = \frac{g'\rho_0}{2}\frac{1}{T}\int_0^T h b^2 dt, \quad (4)$$

where $u'$ and $v'$ are the deviations from the time-averaged velocity fields and $h'$ is the deviation from the time-averaged interface anomaly field. The limits of the periods are here defined as the intervals during which

the total energy remains outside the range of the mean plus or minus one standard deviation (for the high and low energy states) and as the time during which the total energy remains constant to within plus or minus one-half of a standard deviation from the local mean for the intermediate energy case. These definitions will be slightly modified in section 4, but the results do not change significantly.

A striking result is that the mean interface anomaly fields during the three periods of anomalously high energy are visually almost indistinguishable, with root-mean-square (rms) differences of only 3%–8%. Similarly, the mean fields during the two periods of medium energy differ only in some small details, with an rms difference of 7.5%. The mean interface anomaly field during the low energy periods are also quite similar, though some differences are visible and the rms differences are 8%–16%. For comparison, the rms differences between the mean $h$ fields for the high and low energy periods are typically 50%. The mean $h$ fields are presented in Fig. 4 for the first 200 years (the 1000-yr result is visually indistinguishable), the medium energy period of years 158–168, the high energy period of years 23–29, and the low energy period of years 70–74. These averages, each of at least 5 years length, clearly indicate fundamental shifts in the nature of the instability of the free jet. Animation of the streamfunction and relative vorticity fields during each of these periods shows that the high-energy periods are quasi stable—only weak eddies are formed near the eastward extreme of the jet and meanders are very limited. The low-energy periods, in contrast, are characterized by violent meandering and eddy formation in the region just beyond the separation point, so that the existence of a free jet is not always obvious. The medium energy period provides a balance that allows both a penetrating jet and eddy/ring formation.

The long-term mean interface anomaly closely resembles the pattern shown in the medium energy period. The field shows the classic double-gyre pattern, with a standing meander of about 1000-km wavelength on the free jet whose penetration scale is about 1200 km. The primary difference between these two time averages is a spreading of the jet in the long-term mean due to the inclusion of the strongly variable low-energy periods in the time average.

The mean interface anomaly during the high energy period strongly resembles that of the case with no wind asymmetry (McCalpin 1995, Fig. 7). The jet is tightly confined and penetrates approximately 1800 km into the basin, with only a very weak mean meander near $x$ = 1000 km. The ability of the system to largely "ignore" the wind asymmetry in this regime (except for a northward shift of the separation point) is something of a surprise and will be discussed in terms of the time-averaged vorticity balances in section 3c and in terms of eddy–jet interactions in sections 3b and 5.

The mean interface anomaly during the low-energy period shows a third phenomenological regime. The mean jet is significantly spread out meridionally and exhibits a very strong meander of about 800-km wavelength. The penetration scale of the jet is only about 500 km, and the eastward extreme of the mean jet has shifted southward more than 200 km in that distance.

The relation of the streamfunction pattern to the total energy is also visible here. The total energy is dominated by potential energy, which is largely contained in the "pools" on the north and south sides of the free jet in the eastern third of the basin. These "pools" of interface anomaly are largest for the high energy pattern and lowest for the low energy pattern. The kinetic energy of the jet itself is only a small contributor to the total energy and, in fact, is not particularly well correlated with the time-averaged streamfunction patterns.

The differences in the mode and degree of instability of these four time-averaged periods are confirmed by investigation of the eddy kinetic energy fields, Fig. 5. The long-term mean EKE density field shows a maximum EKE extending eastward about 1600 km in a broad band of approximately 500-km meridional extent. This is consistent with a meandering jet creating eddies and rings at a variety of distances from the western boundary. The EKE for the medium energy period is quite similar, except that the maximum is clearly separated from the western boundary, in the 500-km to

1500-km range. Both of these fields show evidence of the standing meander seen in the mean interface anomaly field.

In the high-energy regime, the time-averaged EKE density shows a narrow jet extending zonally across about one-half of the domain before expanding meridionally. The meridionally elongated region about 1350–2000 km from the western boundary indicates that most of the eddy production is limited to this area—meanders and rings are weak or nonexistent. In contrast, the time-averaged kinetic energy density of the low-energy periods occupies a more nearly triangular region extending meridionally about 500 km in each direction from the separation point and outward only 1000 km from the western boundary, with most of the EKE concentrated in the first 600 km.

## b. Stabilization mechanisms

We first consider mechanisms related to the persistence of the high-energy state. Following the example of Holland and Haidvogel (1980), a linear stability analysis (not presented here) was performed to verify that the current system is in a comparable region of parameter space with regard to jet stability. The results were in general agreement with the two-layer QG results of Holland and Haidvogel (1980) and show that the $e$-folding time for unstable wave growth on the
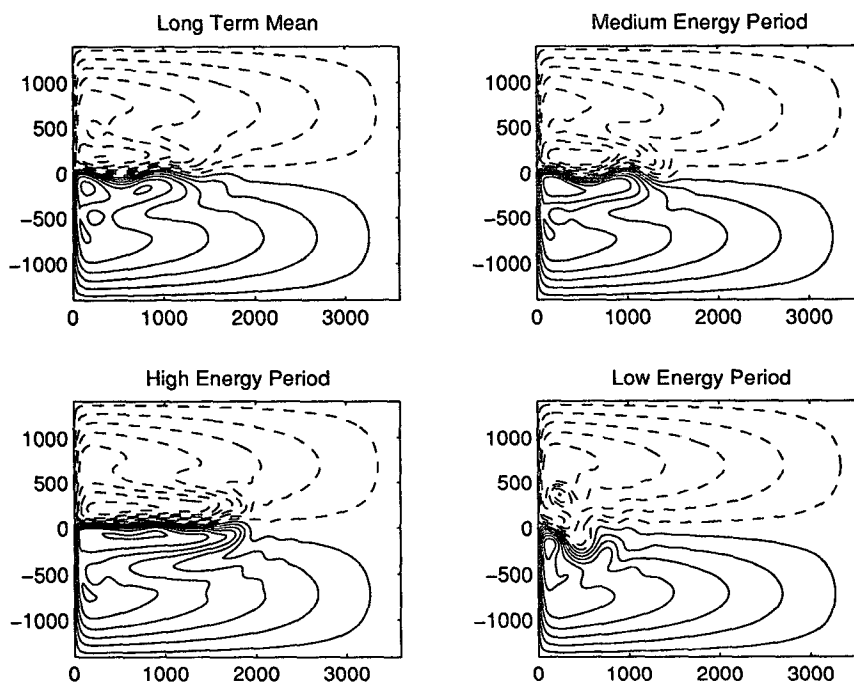


FIG. 4. Time-averaged interface anomaly fields for the reference case. Upper left is for the 200-year record. Upper right is for the medium energy period of years 158–168. Lower left is for the high energy period of years 23–29. Lower right is for the low energy period of years 70–74. All frames employ the same contour interval of 20 m. The axes are horizontal distances in kilometers.
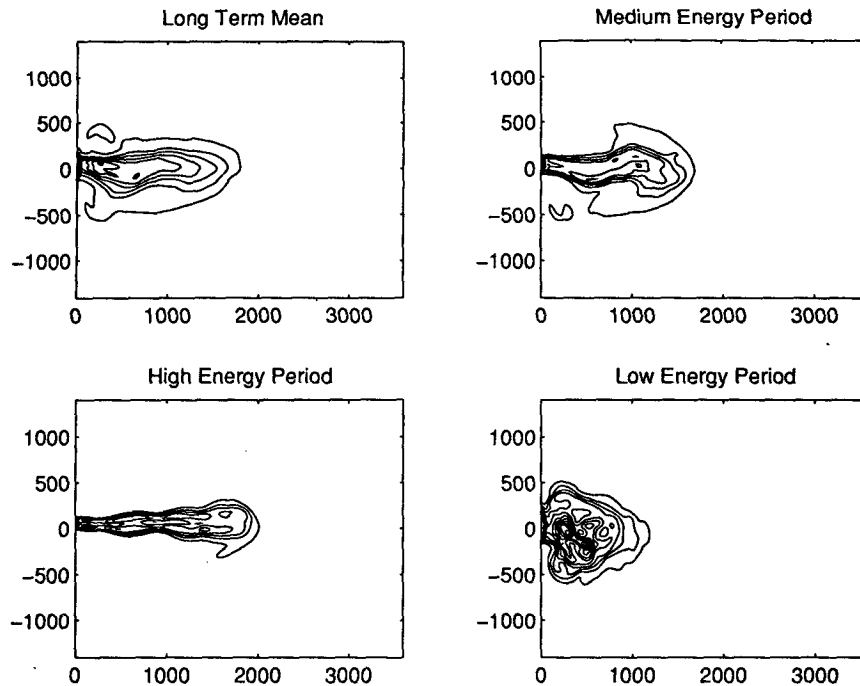
FIG. 5. Time-averaged eddy kinetic energy density fields for the reference case. Upper left is for the 200-year record. Upper right is for the medium energy period of years 158–168. Lower left is for the high energy period of years 23–29. Lower right is for the low energy period of years 70–74. All frames employ the same contour interval and limits. Axes are horizontal distances in kilometers.

mean jet of the high-energy period is in the range of 15–30 days. Since the background noise to excite unstable meanders is not small, it is clear that another mechanism must come into play to override the natural exponential growth tendency of the unstable modes on the free jet and enable the state to persist without the generation of $O(1)$ meanders or rings for periods of 5 years and more.

The dynamical mechanism that arises to maintain the high-energy state is an eddy–jet interaction, which acts to damp meanders. This is demonstrated in Fig. 6, which shows a close-up view of the interaction of a weak, end-generated eddy with a meander. The peak relative vorticity of the eddy in this case is only about 5% of $f_0$. In the top frame, the westward propagating eddy is just beginning to interact with the meander. In the middle frame, the interaction is strong, the eddy entrains some fluid with cyclonic vorticity from the jet, and the meander is straightened out. It is not clear if the entrainment itself or some other process is responsible for the details of the jet's straightening. In the bottom frame, the interaction is almost over, and the meander has been damped except for a residual near the eastern end of the jet. This meander will shortly generate another weak eddy (or two), which will repeat the process. The sequence shown here takes about 3–4 months and is repeated many times during the

high-energy periods. Interactions with both cyclones and anticyclones are seen, with similar effects.

It should be noted that no special phase relationship between the eddy generation and the subsequent meanders is required for this damping mechanism to operate. Since the eddies travel due west (at this level of nonlinearity, self-advective effects are negligible), they will interact with any meanders that happen to form on the jet. Eventually this mechanism fails, and a meander grows to form a ring. When this happens, the anomalous penetration of the free jet decays, and the large pools of potential energy in gyres on the sidelobes of the jet vanish. The timescale for this decay is a bit difficult to quantify, but it appears to be comparable to the 115-day bottom damping timescale and the 200–250-day timescale for Rossby wave propagation from the location of the potential energy peaks to the western boundary.

A nearly opposite mechanism is at work in the maintenance of the low-energy states. During these periods, the free jet experiences very strong meanders and eddy generation in the region just after separation. The rings formed by meander pinch-offs immediately begin interacting with the attached western boundary currents. These interactions cause large meridional excursions in the location of the separation point, which in turn excite large-amplitude meanders in the free jet. Although the
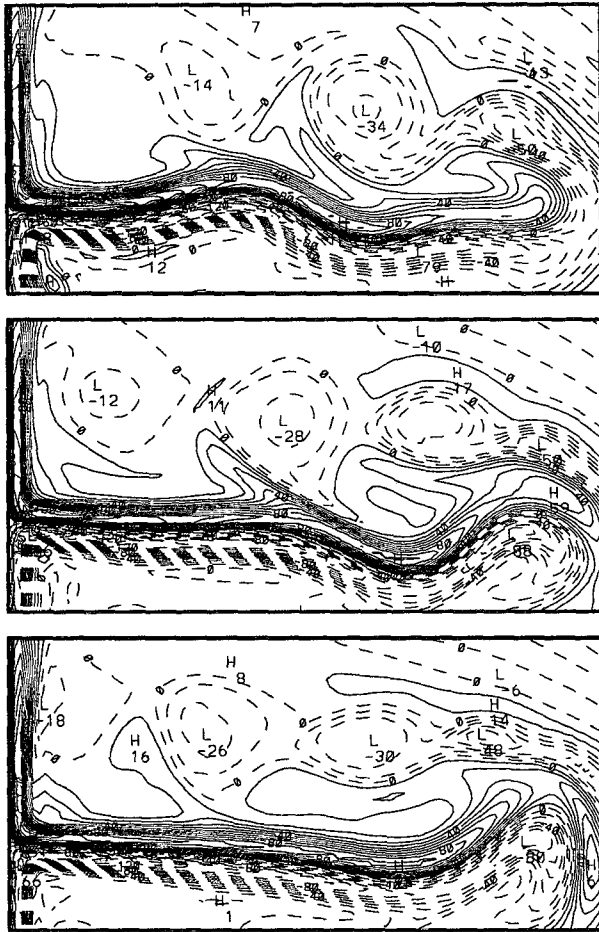
FIG. 6. Close-up of the relative vorticity field during a meander-damping interaction of an eddy with the jet. Top: A growing meander left of center and a westward propagating eddy right of center. Middle: The eddy and meander interact strongly, entraining some of the jet's mass into the eddy. Bottom: After the interaction, the meander is gone, except for a remnant to the east that will soon form another weak eddy.

exact sequences of events are highly complex and irregular, the time-averaged streamfunctions and time-averaged eddy kinetic energy density fields are remarkably similar for each low-energy event. A close-up of the instantaneous relative vorticity field during the first low-energy event, Fig. 7, illustrates the complexity of the flow patterns. The streamfunction field (not shown) suggests that the free jet is following the southern path of cyclonic vorticity, but the potential vorticity field (dominated by the relative vorticity shown here) suggests that the jet is actually bifurcating at the end of the very short zonal segment. In other snapshots, the interactions of strong rings with the attached western boundary currents are so intense that it is impossible to unambiguously identify the existence or location of the jet.

## c. Time-averaged vorticity balances

The time-averaged vorticity equation has often been used to help diagnose and describe the vorticity balances in double-gyre models (e.g., Haidvogel et al. 1992). Applying a time-averaging operator to the governing vorticity equation yields

$$\beta \bar{h}_x = -\frac{g'}{f_0} J(\bar{h}, \nabla^2 \bar{h}) - \frac{g'}{f_0} \overline{J(h', \nabla^2 h')}$$

$$- r\nabla^2 \bar{h} - A_b \nabla^6 \bar{h} + \frac{f_0}{\rho_0 g' H} \text{curl} \vec{\tau}, \quad (5)$$

where $\bar{h}$ is the time-averaged interface anomaly and $h'$ is deviation from the time mean. Although the *global* vorticity balance is dominated by a balance between the interfacial drag and wind stress terms, neither of these terms contribute significantly to the *local* balances in the western boundary current or free jet regions.

The time-averaged vorticity balances from the reference case are of three classes. In the boundary layer (and away from the separation point), there is a three-way balance between lateral viscosity, advection of planetary vorticity, and mean advection of relative vorticity. These results are very similar to those discussed in Haidvogel et al. (1992), and since they are not significantly changed from one phenomenological regime to another, they will not be discussed further here.

Near the separation point, the dominant balance is between eddy and mean advection terms, but the advection of planetary vorticity and lateral viscous terms are not negligible.

It is possible that small changes in these balances could be important in understanding some of the re-

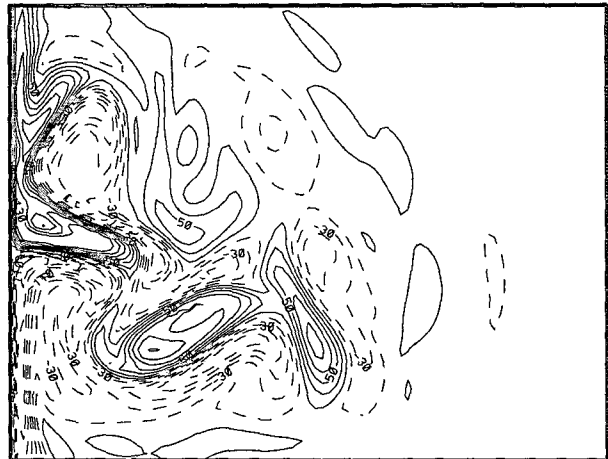Detail of Relative Vorticity During a Low-Energy Period



FIG. 7. A close-up of the instantaneous relative vorticity field during the first low-energy period ($T = 73.42$ years). The domain shown is a 1800 km by 1400 km subset of the full model domain, centered on the separation point latitude.

gimes. For example, the high energy state maintains a nearly zonal free jet that is almost identical to that of the symmetric wind case. One could postulate that a small asymmetry between the boundary layers in the subtropical western boundary current and the subpolar western boundary current could lead to small changes in the integral effect of the viscous terms in the boundary layers. Since the vorticity input differs only by a maximum of 10% between the two gyres in the reference case, it is conceivable that an enhancement of viscosity in the subtropical WBC and a decrease in viscosity in the subpolar WBC could act to cancel out these differences and balance the vorticity on the two sides of the jet. Unfortunately, these hypothetical changes in the vorticity balances are subtle: they are small, they are Lagrangian (i.e., their influence depends on the fluid parcel trajectories), and they are masked by the statistical uncertainties in the time-averaged balances associated with the system's low-frequency variability and our finite time-averaging intervals. As a consequence, we have been unable to unambiguously associate the small changes we observe in the time-averaged vorticity balances in the separation region with changes in the large-scale phenomenology of the system.

In the free jet, the system maintains a two-term balance between mean advection of relative vorticity and eddy advection of relative vorticity. Although this two-term balance is dominant for all three phenomenological regimes of the reference case, the spatial distribution of the fields changes markedly, corresponding to changes in the jet path and penetration.

This two-term balance between eddy and mean advection of relative vorticity is consistent with the stabilization mechanism for the high energy state discussed in the previous section. The small deviations from perfectly zonal structure in the jet give rise to large mean advection of mean vorticity contributions. The jet scale is too wide for either interfacial drag or lateral hyperviscosity to balance these contributions, and the jet is on the line of zero wind stress curl, so that normally small contribution is even smaller at this latitude. The only way for the system to be balanced is by time dependence and the generation of time-averaged perturbation advection of perturbation vorticity. The stabilizing eddy–jet interaction discussed previously is the manifestation of this time dependence.

## 4. Parameter dependence

In order to understand the parametric dependence of the phenomenology described in the previous section, a parameter survey was conducted. The primary parameters varied included the asymmetry parameter for the wind stress and the wind stress magnitude. In addition, the dependence of the solutions on the magnitude of the viscosity and on the grid spacing of the model was briefly investigated. Table 1 shows the portion of pa-

rameter space covered by the main sequence of experiments. Other experiments will be described when they are referenced. The run numbers are provided to allow direct comparison with McCalpin (1995), but we will refer directly to the parameters in most of the following discussion.

The rows in the table are series of increasing wind stress curl asymmetry, while the columns are series with increasing wind stress curl magnitude. A case with weaker winds ($\tau = 0.025$ N m$^{-2}$) had a completely steady solution and will not be discussed further. Runs are of 200 years duration, except runs 105 and 106 are of 125 years duration, and run 115 is of 380 years duration. In each case, the first 10 years were discarded and the analyses were performed on the remainder. Runs 108, 117, and 118 are exceptions—the simulations do not become barotropically unstable for approximately 100 years, so only the last 80 years of the results from each case are used for the analysis. In addition, basin-integrated statistics are available from run 104 for 1000 years of integration and from run 107 for 663 years, but it was not possible to save and analyze the streamfunction fields for the full duration of these runs. All of the runs have total energy time series governed by similar spectra, with cutoff frequencies of about 0.1 cycles per year, though the low-frequency plateau varies in amplitude from case to case.

### a. Dependence on wind stress curl symmetry

For the standard value of wind stress magnitude, a total of nine values of the wind stress curl asymmetry parameter, $\alpha$, were used, with values of 0.00, 0.01, 0.025, 0.050, 0.060, 0.070, 0.080, 0.100, and 0.150. These values define the distribution of the wind stress curl according to (2), as discussed in section 3. Total energy time series for four of the nine cases are presented in Fig. 8. All four series are shown to the same scale in time and energy. The cases with $\alpha = 0.010$ and $\alpha = 0.025$ are visually quite similar to the two cases of small asymmetry shown on the left side of the figure, and the cases with $\alpha = 0.06$, $\alpha = 0.07$, and $\alpha = 0.08$ show a steady transition from the characteristics of the references case ($\alpha = 0.05$) to the case of $\alpha = 0.10$. Aside from the monotonic decrease in the mean as the asymmetry parameter is increased, there are obvious changes in the nature of the variability. There is a systematic increase in the high-frequency variability as the asymmetry is increased and a decrease in the relative occurrence of anomalous high and low energy states. A comparison of the absolute energy values suggests that the symmetric high energy states are actually becoming less common, while the anomalous low energy state is not disappearing but rather coming to dominate the distribution for large values of $\alpha$. The combination of these changes leads to a large decrease in low-frequency variability in the total energy signal for $\alpha = 0.10$ and $\alpha = 0.15$. Despite this general decrease in
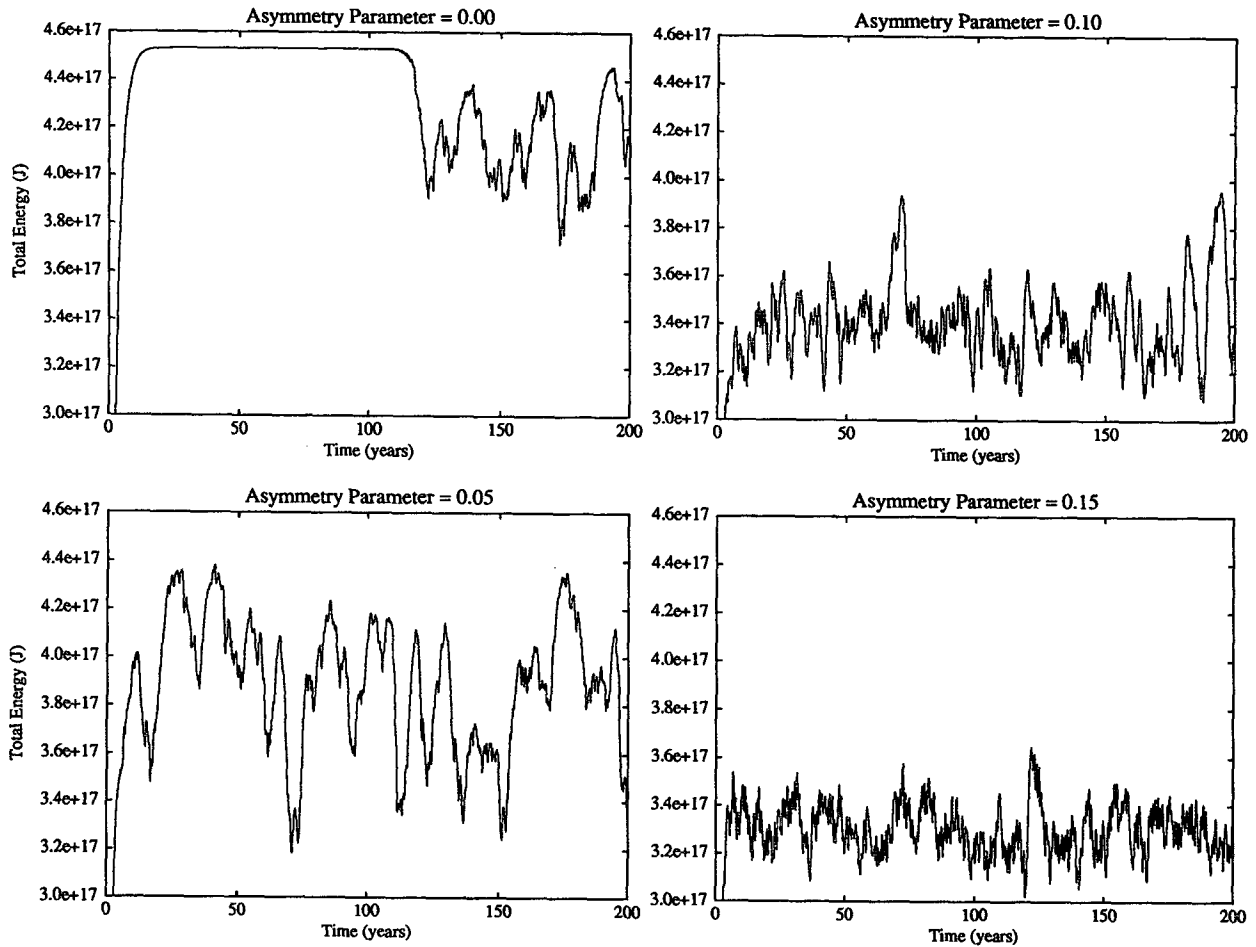
FIG. 8. Time series of total energy for four different values of the wind stress asymmetry parameter.
All plots are to the same scale in time and energy.

low-frequency variability, there are still a small number of extended periods of anomalous high energy for the larger values of $\alpha$.

The behavior of the system as a function of the asymmetry parameter can be seen in a sequence of total energy histograms, Figs. 9 and 10, which present estimates of the probability distribution function of the total energy for each of the nine values of $\alpha$. These two figures show a smooth transition of the system across a series of probability distributions that appear to include three preferred states. For $\alpha \leq 0.010$, the system occupies the high-energy state near $4.3 \times 10^{17}$ J and the medium-energy state near $4.0 \times 10^{17}$ J. As $\alpha$ increases to 0.025, the system is destabilized enough to make brief excursions into the low-energy state near $3.5 \times 10^{17}$ J. For $\alpha = 0.050$ (the reference case), the three states are all commonly occupied. As $\alpha$ is increased past 0.06, the system is no longer able to stabilize the jet in the presence of the strong intergyre asymmetry, and the high-energy state rapidly becomes less common, while the low-energy state even more

rapidly comes to dominate the distribution. By $\alpha$ = 0.100, the original high-energy state is no longer accessible to the system, and even the intermediate energy state is rare. Finally, at $\alpha = 0.150$, the low-energy state is the only one remaining.

To further quantify these effects, we define a measure describing the fraction of the time that the system remains in each total energy range for "long" periods (here defined as exceeding 3.0 years—slightly longer than the time required for a long Rossby wave to cross the basin). Following the general pattern of Figs. 9 and 10 (and paying particular attention to the common location of "gaps" in the distributions), the energy ranges are defined (for the reference value of $\tau$) as

high energy: TE $> 4.25 \times 10^{17}$,
intermediate energy: $3.75 \times 10^{17} <$ TE $< 4.25 \times 10^{17}$,
low energy: TE $< 3.75 \times 10^{17}$.

The results (which are not sensitively dependent on the exact value chosen for the cutoff time scale) are shown
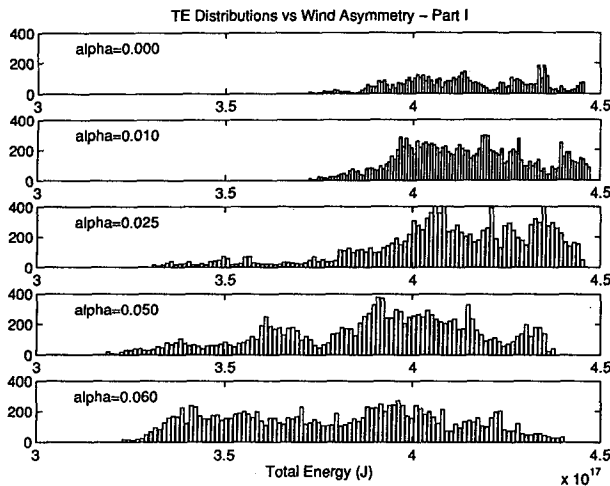
FIG. 9. Histograms of total energy for a series of runs with increasing wind asymmetry parameter, $\alpha$, and fixed wind stress magnitude, $\tau = 0.05$ N m$^{-2}$.



FIG. 10. Continuation of Fig. 9. Histograms of total energy for a series of runs with increasing wind asymmetry parameter, $\alpha$, and fixed wind stress magnitude, $\tau = 0.05$ N m$^{-2}$. The case with $\alpha = 0.06$ is repeated here for clarity.

in Fig. 11. As noted above, the likelihood of the high-energy state decreases rapidly as the wind asymmetry parameter increases to 0.05 and beyond. The intermediate energy state is most common for $\alpha < 0.05$, but its likelihood decreases rapidly for larger asymmetries. The decrease in the fraction of low-energy periods for low values of the asymmetry parameter is apparently associated with the decreased perturbation of the system—without wind asymmetry, the system does not generate sufficiently strong meanders to allow the ring generation characteristic of the low-energy state. The apparent decrease in the fraction of intermediate-energy states as the asymmetry parameter approaches zero is possibly an artifact of insufficient data (only 80 years for $\alpha = 0.00$, compared to 370 years for $\alpha = 0.01$).

The decrease in the proportion of quasi-steady, high-energy states as the asymmetry parameter is increased is due to the difficulty that the system has in maintaining a symmetric, penetrating jet in the presence of such strong asymmetry between the gyres. This asymmetry leads to significant northward shifts in the separation point (about 129 km for $\alpha = 0.15$) and subsequent generation of large meanders in the jet immediately after separation. These meanders are the source of subsequent jet instability.

## b. Dependence on the wind stress magnitude

The changes in behavior of the system with changing wind stress magnitude are generally more subtle than those resulting from changes in the wind symmetry. The time series are visually similar in their variability. For wind stress values of 0.075 and 0.100 N m$^{-2}$, the histograms of total energy (not shown) display the same pattern as for the reference case as the asymmetry
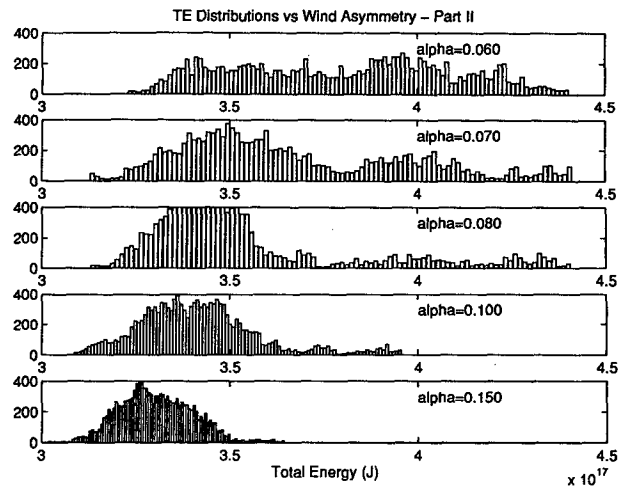
parameter is increased. In particular, the sharp transition occurs between $\alpha = 0.05$ and $\alpha = 0.10$ for all three values of the wind stress magnitude. The primary differences are that the distributions are broader for small values of $\alpha$ in the cases with stronger winds, and the distributions are not as clearly separated into distinct modes as in the case with $\tau = 0.050$ N m$^{-2}$. They display some "gaps," but these are smaller and less consistently located than for the reference value of the wind stress. The broadened distributions reflect the decreased stability of the system as the nonlinearity is increased and its consequent increased ability to occupy the low-energy state.
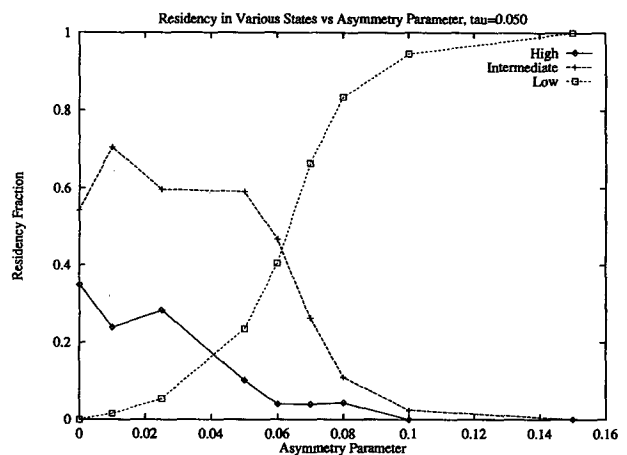


FIG. 11. Fraction of the time during which the system remains in a given energy range for longer than 3 years, as a function of the wind asymmetry parameter. The wind stress magnitude is fixed at 0.05 N m$^{-2}$. The energy ranges are defined in the text.

Using the reference asymmetry parameter, $\alpha = 0.050$, we studied the total energy histograms and chose the energy range limits as $0.97 \times 10^{18}$ and $1.15 \times 10^{18}$ J for $\tau = 0.075$ and $1.87 \times 10^{18}$ and $2.25 \times 10^{18}$ J for $\tau = 0.100$. Again using 3 years as the definition of "long," the fraction of the simulation that is spent in long periods of the three total energy ranges is presented in Fig. 12. As the wind stress is increased, we see that the quasi-steady, high-energy states decrease and vanish. This is apparently a joint effect of increasing nonlinearity and nonzero wind stress asymmetry, since the high-energy states do not vanish as the wind stress increases for smaller values of $\alpha$. We conclude that the effects of increased wind stress asymmetry and increased wind stress magnitude are in some sense additive factors in destabilizing the high-energy states. Unfortunately, the rather subjective nature of the definitions of the ranges of the anomalous energy regimes precludes further quantitative comparisons here.

A general change in the phenomenology that is not easily seen in the total energy distributions is a rapid (i.e., faster than quadratic) increase in total energy as the wind stress magnitude is increased. The increase comes from a combination of increased jet penetration and increased gyre strength because increased penetration allows the (potential energy defining) thermocline anomaly pools on the north (south) sides of the free jet to be longer as well as shallower (deeper). The change in mean penetration is also evident in the first moment of the kinetic energy distribution, which increases from 600 km to 1000 km as the wind stress magnitude is increased from 0.05 to 0.10 N m$^{-2}$ (as discussed in McCalpin 1995).

### c. Dependence on numerical parameters

A few tests were run to make sure that the results obtained were not unduly sensitive to the particular choice of numerical parameters used here. We found that decreasing the lateral biharmonic viscosity from 8 $\times 10^{10}$ m$^4$ s$^{-1}$ to 2 $\times 10^{10}$ m$^4$ s$^{-1}$ decreased both the occurrence of the high-energy state (from 10% to 2.5%) and the occurrence of the low-energy state from (23% to 13%). The decrease of the high-energy state is consistent with the expectation that decreased viscosity would lead to destabilization of the free jet. The cause of the decrease in the low energy state is not clear; the total energy histogram shows that low-energy periods still occur, but they are less common than in the reference case. Further reductions of the viscous coefficient result (at this grid spacing) in noisy solutions that are not useful simulations of the continuum governing equation.

The results are somewhat sensitive to the grid spacing of the model. Decreasing the grid spacing from 20 to 10 km (using a lateral biharmonic viscosity parameter of 2 $\times 10^{10}$ m$^4$ s$^{-1}$ for both cases) produced a shift toward higher energies in the total energy histogram
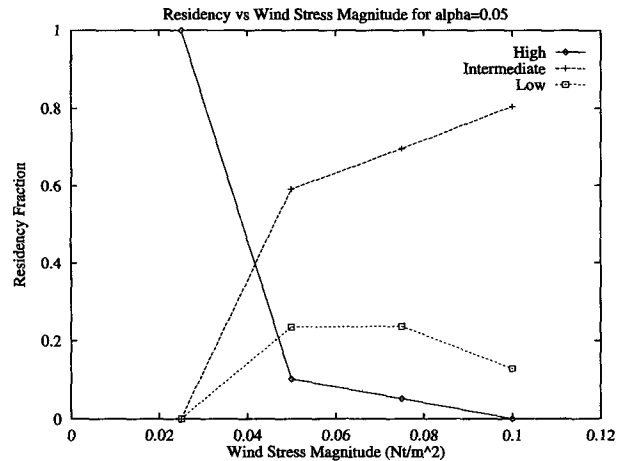


Residency vs Wind Stress Magnitude for alpha=0.05

FIG. 12. Fraction of the simulation during which the system remained in a given energy range for longer than 3 years, as a function of the wind stress magnitude, for a fixed wind asymmetry of 0.050.

and (relative to the 20-km case with the same viscosity) an increase in the occurrence of the high-energy state (from 2.5% to 7%), with essentially no change in the occurrence of the low-energy state. The shift toward higher values of total energy, while not regarded as statistically significant in McCalpin (1995), is associated with a statistically significant increase in the mean penetration scale (defined as the first moment in $x$ of the kinetic energy density distribution) from 600 km to slightly over 800 km. This comparison is interesting, because it is consistent with the observation of Barnier et al. (1991), who obtained greatly increased jet stability and penetration in their six-layer QG model when the resolution was changed from 20 to 10 km. This change in behavior is probably related to slow convergence of the finite-difference schemes in representing the approximate discontinuity in relative vorticity that is present along the central axis of the jet, as discussed by Marshall and Marshall (1992), as well as the slow convergence of the discretization of the narrow viscous boundary layers (Haidvogel et al. 1992).

Finally, one case was run with standard wind stress and wind asymmetry parameters but with reduced bottom drag ($r = 0.5 \times 10^{-7}$ s$^{-1}$, instead of $r = 1.0 \times 10^{-7}$ s$^{-1}$). One might expect this to provide results similar to those with increased wind stress, but instead the simulation behaves like the cases with increased wind asymmetry (very similar to $\tau = 0.050$, $\alpha = 0.100$ of Fig. 9, though with a 60% higher mean energy level). This phenomenology is in accord with our theory of the governing dynamics discussed in the following section.

## 5. Discussion

### a. Comparison with other studies

Two recent studies have investigated multiple equilibrium solutions for double-gyre models. Cessi and

Ierley (1995) find steady solutions to the barotropic QG equations for this system. In addition to symmetric solutions, they find some asymmetric solutions that come in mirror-image pairs. They show that the antisymmetric solution is generally stable when the scale of the inertial boundary layer is smaller than that of the Munk layer and that a pair of nonsymmetric solutions are stable when these boundary-layer scales are close to equality. Multiple stable equilibria only exist in a very small portion of parameter space for finite and approximately equal inertial and viscous boundary-layer scales. Comparisons with their results are complicated by the differing dynamical approximations and viscous parameterizations and by the different regions of parameter space explored. For our system, the viscous boundary-layer scale is obtained by equating the biharmonic viscous and planetary vorticity terms (note that the interfacial drag term is negligible at these scales):

$$L_M = \left(\frac{A_b}{\beta}\right)^{1/5}. \tag{6}$$

The advective boundary-layer scale is obtained by equating the advective and relative vorticity terms

$$L_I = \left(\frac{L_x}{L_y}\frac{\text{curl}\vec{\tau}}{\rho_0\beta^2 H}\right)^{1/2}, \tag{7}$$

where $L_x$ and $L_y$ are the basin dimensions in the $x$ and $y$ directions, respectively. These formula correspond to (2.2) and (2.3) of Cessi and Ierley.

For our reference parameters, we obtain a dimensional viscous boundary-layer scale of 21 km and a dimensional advective boundary layer scale of 24 km. The nondimensional values of 5.8 × 10$^{-3}$ and 6.7 × 10$^{-3}$ are a factor 2–3 smaller than any presented by Cessi and Ierley. Extrapolating from their Fig. 7 suggests that our parameters correspond to a region of parameter space where their model would be expected to have no stable equilibria, but with the possibility of five or seven unstable equilibria (depending on exactly how the curves behave outside the parameter space they explored). This is consistent with the strongly time-dependent behavior exhibited by our model.

A second paper presenting the results of similar work is Jiang et al. (1995). They applied a reduced-gravity shallow-water model to the double-gyre system and found multiple stable equilibrium solutions by time integration from different initial conditions. Their paper is particularly relevant to our study because the reduced-gravity shallow-water equations have Rossby wave phase speeds closer to ours than the barotropic model of Cessi and Ierley (1995). In addition, the shallow-water equations are not precisely symmetric and deviations in the upper-layer thickness will introduce asymmetries at the order of the Rossby number. Despite this dynamical asymmetry, Jiang et al. discover

multiple equilibrium solutions that are almost mirror-image pairs. Since these mirror-image pairs have the same energy, we would not expect to see them in the analysis of total energy presented here.

We looked for evidence of multiple equilibrium solutions by studying the distribution of the location of the separation point. Since the mirror-image pairs have separation points located on opposite sides of the location of zero wind stress curl, one would expect to find a bimodal distribution of separation points if these solutions were present. We found no evidence of bimodality in the separation point histograms for any of the parameters investigated here. In every case, the quasi-steady solution was nearly exactly antisymmetric. In cases with wind asymmetry, the deviations from antisymmetry in the time averages of the quasi-steady solutions were of the same form for each occurrence.

There are a variety of reasons why we may not have seen the multiple equilibrium solutions here. Most importantly, our cases are generally in a much more nonlinear part of parameter space for which the equilibrium solutions may be unstable. Although it is difficult to compare the runs quantitatively, due to the differences in geometry and subgrid-scale viscous mechanisms, the present cases have about twice the Sverdrup transport, twice the bottom drag, and about one-half the lateral viscosity (for deformation radius scales) compared to those of Jiang et al. (1995). Also, the current experiments used exclusively free-slip boundary conditions in a rather large domain, while the multiple equilibrium solutions obtained by Jiang et al. were for the case of no-slip boundaries in a much smaller domain. These latter changes both act to destabilize the steady solutions in our cases and may change the separation points of the multiple equilibrium solutions so that their existence might not be clear in that signal even if they were present.

Although we did not find evidence of multiple *equilibrium* states, there is strong evidence of multiple *preferred total energy levels*. In general, these are one high-energy quasi steady state, one intermediate-energy eddy-containing state, and one low energy weakly penetrating state. In the extremes of parameter space, these merge into one or two states that come to dominate the total energy histogram.

The high-energy state is characterized by a strong and straight free jet whose instability is countered by numerous eddy–jet interactions that damp the growing meanders. The low-energy state is characterized by strong meanders and ring formation. These rings disrupt the western boundary currents and cause more strong meanders and rings. The intermediate-energy state has a mix of end-generated eddies and meander-generated rings.

We have found no evidence of large-scale, quasi-periodic behaviors underlying the low-frequency variability (which would perhaps be more appropriately

referred to as "long timescale variability") and con-
clude that it is a dominated by a Fourier projection of
the irregularly spaced transitions between states. Figure
13 shows the *dominant* state as a function of the wind
stress magnitude and wind stress asymmetry parame-
ters. The low-frequency variability is greatest in the
region near the reference parameters, for which all
three states are admissible.

### b. Dynamical mechanisms

We note that the low-frequency variability of the
system is strongly enhanced by the persistence of these
regimes and the irregular transitions between them.
Therefore, the key to understanding the low-frequency
variability of the system is contained in the stabilization
mechanisms that allow the persistence of the various
states. Although certain aspects of the behavior of the
system are too complex to allow definitive answers at
this time, we hypothesize that it is the variation in the
strength of the eddy–boundary current interactions that
provides the fundamental mechanism that allows both
the observed diversity of behavior and the observed
persistence of each phenomenological regime.

Let

$$T_{drift} = \frac{L}{c} \qquad (8)$$

be the time required for an eddy or ring to travel west-
ward from its creation at $x = L$ to the western boundary.
Then let $T_{diss}$ be the dissipative timescale for the eddy.
Consider the following three cases.

- $T_{drift}/T_{diss} \ll 1$: The ring is formed soon after the
separation of the free jet, so it will be strong when it
interacts with the western boundary current. The inter-
action will generate significant meanders and more
rings and hence a persistent low-energy state.

- $T_{drift}/T_{diss} \gg 1$: The eddy is generated near the east-
ward extreme of the jet and it decays substantially dur-
ing its drift to the western boundary. It will not generate
new meanders in that interaction. In addition, it will
have acted to damp meanders in the free jet by the
mechanism illustrated in Fig. 6, thus producing the per-
sistent high-energy state.

- $T_{drift}/T_{diss} \approx 1$: The eddy is formed near the middle
of the jet. It is neither strong nor of negligible energy
when it interacts with the western boundary current,
and the resulting interaction will generate modest me-
anders and lead to modest instability with a correspond-
ing intermediate energy level.

For the model parameters and observed eddy scales,
the decay due to the biharmonic viscosity is negligible
compared to that due to the ad hoc interfacial drag.
Similarly, applying the results of Smith and Reid
(1982) (their Fig. 8, with $\gamma = 2$ for these relatively
large eddies and $Q^* = 6.67$ for the weakest of the ed-
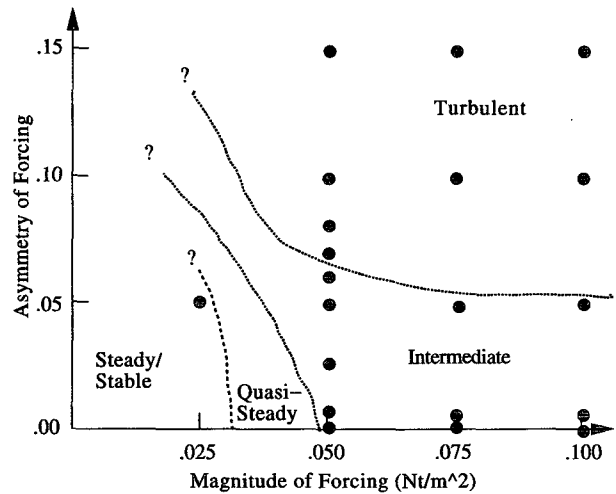dies observed here) shows that dispersive effects are



FIG. 13. Dependence of the *dominant* mode of the system as a function
of the wind stress magnitude and wind stress asymmetry parameters.
Circles indicate parameters of simulations run, as shown in Table 1.

also smaller than the interfacial drag damping. Thus
$T_{diss}$ may be considered fixed at $r^{-1} = 10^7$ s ($=116$
days).

The parameter $T_{drift}$ will vary depending on both the
location of the eddy generation and the effective drift
speed. To estimate the location of eddy generation, $L$,
we make use of the maps of eddy kinetic energy density
(e.g., Fig. 5) during each period. The drift speed is the
sum of the large-scale advection and the $\beta$-induced west-
ward drift. To determine the correct value we analyzed
several case studies, both by visual tracking of eddy cen-
ters and by calculating slopes of contours of $x-t$ plots
of the streamfunction for fixed $y$ values. From these, we
conclude that the effective drift speed is typically within
10% of the phase speed of long Rossby waves, $-\beta R_d^2$
$= 0.045$ m s. Since this is simply an order of magnitude
scaling estimate, we therefore use the long Rossby wave
phase speed in the calculation of $T_{drift}$.

For the high energy periods, the eddy-generation re-
gion is in the range from 1350–2000 km, so $T_{drift}$ is
between 350 and 520 days, leading to $T_{drift}/T_{diss} = 3.0–$
4.5. For the low-energy periods, the eddy/ring gener-
ation region is the area from 200–550 km, leading to
$T_{drift}$ in the range of 50–150 days or $T_{drift}/T_{diss}$ in the
range 0.44–1.30. An eddy kinetic energy map from the
intermediate-energy period from years 155–169 shows
a broad peak of eddy kinetic energy from 525–1050
km, which lies between the eddy-generation locations
of the extreme energy periods. Corresponding values
of $T_{drift}/T_{diss}$ are 1.30–2.60. These values are in very
good agreement with the expectations and provide a
very simple way to categorize the type and importance
of the eddy–jet interactions.

This categorization also explains the behavior of the
case with reduced bottom drag discussed in section 4c.
Even though the asymmetry of the forcing is weak, the

system is strongly dominated by a low-energy, moderately penetrating state, with only occasional transitions into higher-energy states. The decreased interfacial friction parameter leads to significantly reduced eddy damping, stronger eddy–jet interactions, and thus less jet penetration and less total energy.

Despite this qualitative agreement with our hypothesis, this characterization of the system provides no explanation of the *separation* between the peaks of the histograms (Figs. 2, 9, 10), and no clear explanation is currently available. Since this separation is most clear for the cases with the weakest nonlinearity, it is possible that this feature is related to some aspect of the set of steady (but typically unstable) solutions to the system (Cessi and Ierley 1995; Jiang et al. 1995), but more work is needed to clarify the relationship (if any) this far into the aperiodic solution regime.

We note that this parameterization of the regimes of total energy is only relevant in the case for which the eddies are expected to provide the major source for the generation of meanders. In the cases with increased wind asymmetry, for example, the meanders are generated more or less continuously, and this characterization is less relevant.

## 6. Summary

The simple double-gyre model described here and used in a variety of basic dynamical studies has been shown to contain significant and dynamically interesting low-frequency variability. This low-frequency variability is attributable to infrequent and irregular transitions of the system into (and out of) a small number of preferred states, which can be characterized by differing ranges of total energy. The existence of these multiple states appears to be related to our choice of a parametric regime in which the viscous decay of an eddy/ring before its interaction with the western boundary current can be anywhere from negligible to large.

The existence of multiple preferred states in the total energy distribution generally decreases as the parameters get farther away from those leading to an antisymmetric stable state. We discovered no evidence of traditional multiple equilibria, especially in the separation point statistics (Cessi and Ierley 1995; Jiang et al. 1995).

The dependence of the low-frequency variability on the existence of the multiple preferred states produces some counterintuitive results concerning the parameter dependence of the low-frequency variability. In particular, increasing the nonlinearity initially acts to *increase* the low-frequency variability by making the solution first unsteady, then capable of multiple persistent states. As the nonlinearity is further increased, the low-frequency variability is *decreased* as the higher-energy states cease to occur often enough to contribute significant variance to the signal. In a similar manner, increasing the wind asymmetry initially *increases* the low-frequency variability by perturbing the system sufficiently to allow low-energy,

weakly penetrating states. As the wind stress asymmetry is further increased, the low-frequency variability is *decreased* as the system becomes too strongly asymmetric to sustain the higher energy, more penetrating states. These results may have important implications for marginally eddy-resolving models (i.e., those run with moderate resolution and relatively large viscosity), since they may be parametrically close to steady viscous solutions.

REFERENCES

Barnier, B., B. Lien-Hua, and C. LeProvost, 1991: On the catalytic role of high baroclinic modes in eddy-driven large-scale circulations. *J. Phys. Oceanogr.,* **21,** 976–997.

Bryan, K., 1963: A numerical investigation of a nonlinear model of a wind-driven ocean. *J. Atmos. Sci.,* **20,** 594–606.

Cessi, P., and G. Ierley, 1995: Symmetry-breaking multiple equilibria in quasigeostrophic, wind-driven flows. *J. Phys. Oceanogr.,* **25,** 1196–1205.

Chassignet, E., and P. R. Gent, 1991: The influence of boundary conditions on midlatitude jet separation in ocean numerical models. *J. Phys. Oceanogr.,* **21,** 1290–1299.

Haidvogel, D. B., J. C. McWilliams, and P. R. Gent, 1992: Boundary current separation in a quasigeostrophic, eddy-resolving ocean circulation model. *J. Phys. Oceanogr.,* **22,** 882–902.

Holland, W. R., 1973: Baroclinic and topographic influences on the transport in a western boundary current. *Geophys. Fluid Dyn.,* **4,** 187–210.

——, 1978: The role of mesoscale eddies in the general circulation of the ocean—numerical experiments using a wind-driven quasigeostrophic model. *J. Phys. Oceanogr.,* **8,** 363–392.

——, and D. B. Haidvogel, 1980: A parameter study of the mixed instability of idealized ocean currents. *Dyn. Atmos. Oceans,* **4,** 185–215.

Jiang, S., F.-F. Jin, and M. Ghil, 1995: Multiple equilibria, periodic and aperiodic solutions in a wind-driven, double-gyre, shallow-water model. *J. Phys. Oceanogr.,* **25,** 764–786.

Marshall, D., and J. Marshall, 1992: Zonal penetration scale of midlatitude oceanic jets. *J. Phys. Oceanogr.,* **22,** 1018–1032.

McCalpin, J. D., 1987: On the adjustment of azimuthally perturbed vortices. *J. Geophys. Res.,* **92,** 8213–8225.

——, 1995: The statistics and sensitivity of a double-gyre model: The reduced-gravity, quasigeostrophic case. *J. Phys. Oceanogr.,* **25,** 806–824.

McWilliams, J. C., N. J. Norton, P. R. Gent, and D. B. Haidvogel, 1990: A linear balance model of wind-driven, midlatitude ocean circulation. *J. Phys. Oceanogr.,* **20,** 1349–1378.

Rhines, P. B., and R. Schopp, 1991: The wind-driven circulation: Quasigeostrophic simulations and theory for nonuniform winds. *J. Phys. Oceanogr.,* **21,** 1438–1469.

Smith, D., and R. O. Reid, 1982: A numerical study of nonfrictional decay of mesoscale eddies. *J. Phys. Oceanogr.,* **12,** 244–255.

Veronis, G., 1966: Wind-driven ocean circulation—Part 2. Numerical solutions of the non-linear problem. *Deep-Sea Res.,* **13,** 31–55.

Verron, J., and C. LeProvost, 1991: Response of eddy-resolved general circulation numerical models to asymmetrical wind forcing. *Dyn. Atmos. Oceans,* **15,** 505–533.

——, ——, and W. R. Holland, 1987: On the effects of a midocean ridge on the general circulation: Numerical simulations with an eddy-resolved ocean model. *J. Phys. Oceanogr.,* **17,** 301–312.